

ARTICLE

<https://doi.org/10.1038/s42004-019-0201-9>

OPEN

Amorphous 2D materials containing a conjugated-polymer network

Shoichiro Yano¹, Kosuke Sato¹, Jumpei Suzuki¹, Hiroaki Imai¹ & Yuya Oaki^{1,2} 

Two-dimensional materials, such as layered compounds and nanosheets, have attracted interest for their characteristic structures and properties. If layered materials containing functional organic molecules are synthesized, designed nanosheets can be obtained by exfoliation. Here we show the design and synthesis of an amorphous organic layered material containing a conjugated-polymer network, its exfoliation into nanosheets, and their applications. Copolymerization of benzoquinone and pyrrole generates random stacks of the conjugated polymer layers through successive C-C bond formation and pericyclic reaction under mild conditions at 60 °C. The amorphous organic layered materials are efficiently exfoliated into nanosheets in 44.6% after 1 h. The nanosheets are used as a metal-free electrocatalyst for hydrogen evolution reaction with the overpotential 0.28 V (vs. RHE). The present approach may be applied to the design of functional nanosheets with graphene-like structures under mild conditions.

¹Department of Applied Chemistry, Faculty of Science and Technology, Keio University, 3-14-1 Hiyoshi, Kohoku-ku, Yokohama 223-8522, Japan. ²PRESTO, Japan Science and Technology Agency (JST), 4-1-8 Honcho, Kawaguchi 332-0012, Japan. Correspondence and requests for materials should be addressed to Y.O. (email: oakiyuya@aplc.keio.ac.jp)

Two-dimensional (2D) materials are found in a variety of inorganic and organic compounds^{1–6}. Nanosheets are obtained by exfoliation of layered structures in the liquid phase. The enhanced properties and emergent functions of such materials are derived from their characteristic nanostructures, such as large specific surface area, flexibility, and anisotropic shape^{1–11}. If desired functional molecules are polymerized and embedded in nanosheets, the functional units can be effectively used without aggregation and dissolution. In this work, we synthesize organic nanosheets containing benzoquinone (BQ) and pyrrole (Py) moieties (BQ–Py nanosheet) through exfoliation of the precursor amorphous layered materials (Fig. 1). The BQ–Py nanosheets show enhanced electrocatalytic performance for hydrogen evolution reaction (HER).

A variety of exfoliation methods and processes have been studied for layered materials^{1,12–16}. Layered compounds consisting of the layers stacked via van der Waals interaction, such as graphite, boron nitride, and metal dichalcogenides, are exfoliated into nanosheets in liquid phase with application of certain stimuli¹². Layered structures consisting of the charged layers and interlayer ions are found in clays and transition-metal oxides. These layered compounds are delaminated by intercalation of bulky ion and subsequent osmotic swelling with dispersion medium¹³. Layered composites of inorganic layers and interlayer organic guests are exfoliated into nanosheets on the basis of the affinity between the guest and dispersion medium^{14–16}. In recent years, a new family of 2D materials have been synthesized, such as metal-organic and covalent-organic frameworks (MOFs and COFs) and carbon nitrides^{17–21}. These 2D materials contain the desired functional units in the layers. MOFs and COFs with layered structures have been exfoliated into nanosheets^{22–25}. However, it is not easy to exfoliate these frameworks in high yield and efficiency²². Recently several methods, such as liquid phase, mechanical, and charged exfoliation, were applied to COFs^{23–25}. In our recent paper, exfoliation efficiency, such as the time and

yield, in previous papers were summarized in a figure¹⁶. Although high-yield exfoliation of graphitic carbon nitride, graphite, and transition-metal dichalcogenides was reported with the specific time and yield, such as 70% for 0.5 h, the specific values were not found for the recent framework materials. Our intention here is to prepare the low-crystalline 2D structures in both lateral and vertical directions to study the exfoliation behavior. Although amorphous states were observed in frameworks and layered materials^{26–33}, the amorphous nature was not applied to the exfoliation. A recent report shows that grafting of bulky alkyl chains on the layer of a COF induced smooth exfoliation into the nanosheets³⁴. If amorphous organic layered materials consisting of noncrystalline layers and their random stacks are synthesized, the nanosheets can be obtained by efficient exfoliation.

Quinone derivatives are used as an organic oxidant for synthesis and active material for energy storage^{35,36}. In our previous works, high-yield synthesis of polypyrrole (PPy) was achieved on the crystal surface of quinone derivatives through oxidative polymerization with diffusion of the monomer vapor^{37,38}. The substituents on the α position of quinone derivatives were required for synthesis of PPy because the lack of the substituents caused side reactions other than oxidative polymerization. In this study, we found that BQ without substituents induces the simultaneous reactions with Py in two different schemes, such as the C–C bond formation and pericyclic reaction (Fig. 1a, b), forming the amorphous 2D polymer layers and their random stacks at 60 °C under ambient pressure (Fig. 1c, d). Although the individual reaction scheme was reported for synthesis of dye molecules from naphthoquinone (NQ) and Py derivatives^{39,40}, the successive reactions were inhibited by protecting groups on the quinone and Py rings.

In recent years, a variety of HER catalysts have been studied to alternate platinum^{41–64}. Heteroatom-doped graphene and graphitic carbon nitride showed high electrocatalytic activity as metal-free HER catalyst^{46–64}. Previous works indicate that Py and pyridine moieties in 2D graphitic layers serve as the active sites for HER^{41–44}. Since large amount of Py rings are contained in the BQ–Py polymer layers, the enhanced catalytic properties are expected for the nanosheets exhibiting the active site. These results imply that a variety of functional nanosheets can be obtained by synthesis and exfoliation of amorphous layered materials.

Here we report the synthesis of amorphous polymer layers containing a conjugated network and their random stacks containing BQ and Py moieties through successive reactions at 60 °C (Fig. 1). Spontaneous reactions with different schemes and rates in 2D direction play important roles for formation of the amorphous layered materials. The resultant amorphous layered materials are efficiently exfoliated into nanosheets in liquid phase. Moreover, the resultant BQ–Py polymer nanosheets are applied to a metal-free electrocatalyst for HER.

Results

2D Conjugated-polymer network through consecutive reactions. Powder of BQ (30 mmol) and liquid of Py (30 mmol) were separately set in a closed vessel at 60 °C for 48 h under ambient pressure (Fig. 2a). Vapor of Py monomer was supplied to solid-state BQ powder. The detailed procedure was described in the Method. The color of BQ powder was changed from yellow to black (Fig. 2a, b). The resultant powder was purified by washing with acetone and then vacuum-dried to remove the remaining monomers and oligomers. The bulky particles around several-tens micrometer in size were observed on the images of scanning electron microscopy (SEM) (Fig. 2b). The resultant material had the different structure from the reference compounds, such as

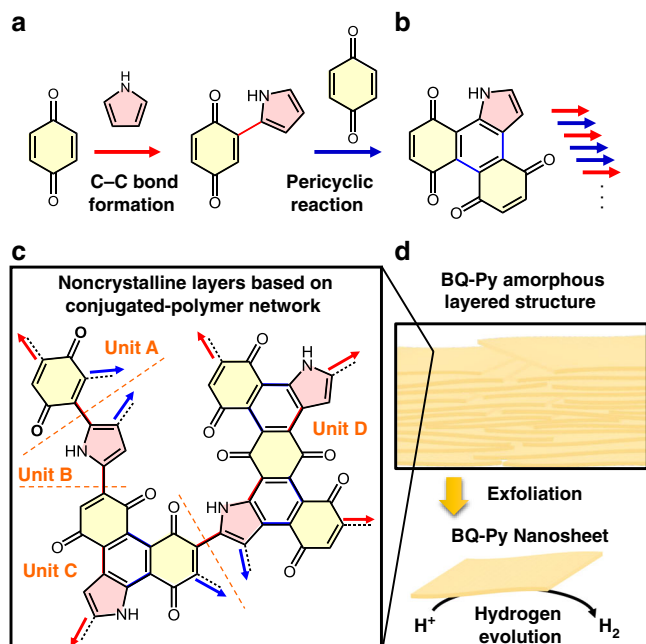


Fig. 1 Schematic illustration for synthesis of amorphous organic layered material. **a, b** Successive C–C bond formation (red arrow) and pericyclic reaction between BQ and Py (blue arrow). **c** Four structure units of BQ–Py polymer in the noncrystalline layers. **d** Amorphous layered structure and its exfoliation into the nanosheets with the enhanced catalytic properties for electrochemical hydrogen evolution reaction (HER)

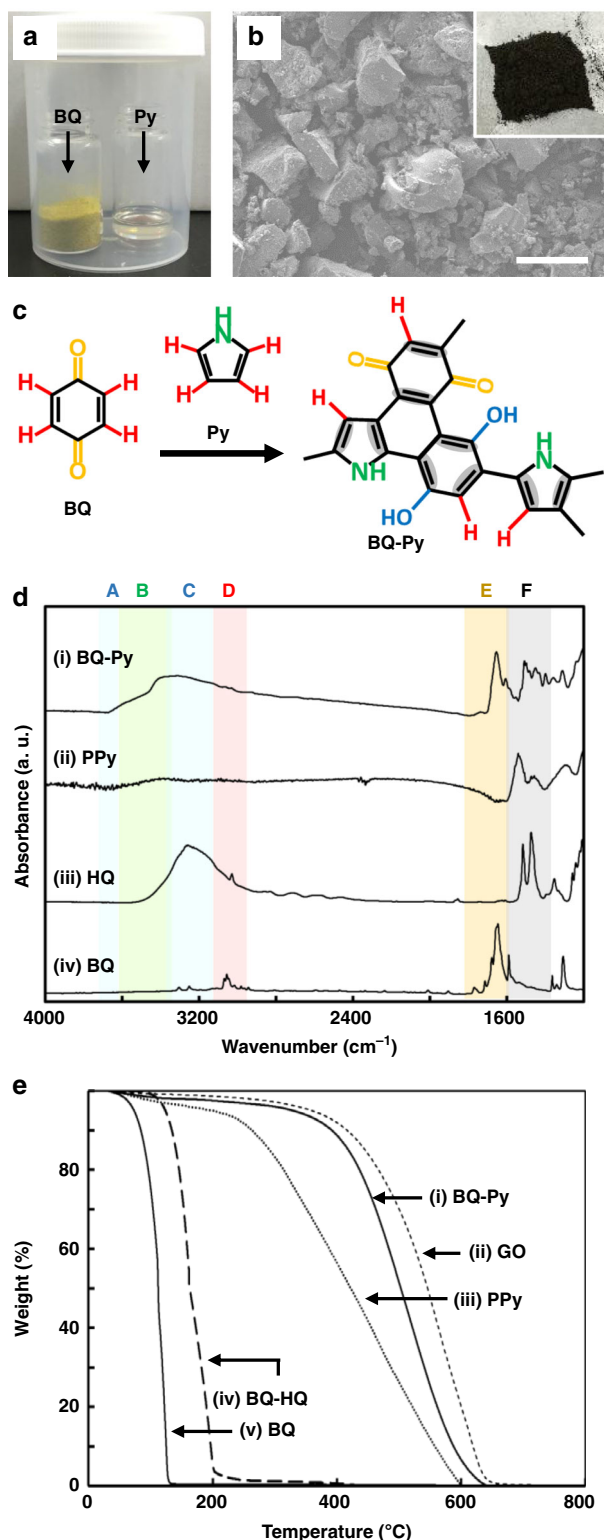


Fig. 2 Synthesis and characterization of amorphous layered BQ-Py polymer. **a** Photograph of the experimental setup. **b** Photograph (the inset) and SEM image of the resultant powder. **c** Representative molecular structures for interpretation of the FT-IR spectrum. The colors correspond to those in the panel **(d)**. **d** FT-IR spectra of the BQ-Py polymer (i), PPy (ii), HQ (iii), and BQ (iv). **e** TG curves of the BQ-Py polymer (i), graphene oxide (GO) (ii), PPy (iii), charge-transfer complex of BQ and HQ (BQ-HQ) (iv), and BQ (v). The scale bar for **(b)** represents 100 μm

commercial BQ, hydroquinone (HQ), their charge-transfer complex (BQ-HQ), and PPy, on Fourier-transform infrared (FT-IR) absorption spectra, thermogravimetric (TG) curve, and X-ray diffraction (XRD) pattern (Figs. 2c–e and 3a). FT-IR spectra support formation of the BQ-Py network as shown in Fig. 2c, d. The resultant BQ-Py polymer shows the absorption bands of N–H stretching, C = O stretching, and C = C stretching vibrations corresponding to BQ and Py rings (the bands B (green), E (yellow), and F (gray), respectively, for the spectrum (i) in Fig. 2c, d). In contrast, not all these three absorptions were detected on the reference compounds (the spectra (ii–iv) in Fig. 2d)). The absorption corresponding to C–H stretching vibration on aromatic ring was weakened for the BQ-Py polymer compared with BQ and HQ monomers because of the condensation of BQ and Py rings (the band D (red) for the spectrum (i) in Fig. 2c, d). The appearance of O–H stretching vibration is ascribed to the presence of HQ moiety and hydrated water in the BQ-Py polymer (the bands A and C (blue) in Fig. 2d). Formation of the BQ-Py polymer with the estimated structure was also supported by X-ray photoelectron spectroscopy (XPS) and ^{13}C nuclear magnetic resonance (NMR) spectroscopy (Supplementary Figs 1 and 2). The Raman spectroscopy showed the broadened peak around 1350 and 1590 cm^{-1} corresponding to D and G bands, respectively (Supplementary Fig. 1). The BQ-Py polymer showed the higher peak intensity ratio of the D to G bands than a commercial stacked graphene and graphene oxide. The Raman spectra imply formation of the graphitic amorphous BQ-Py layers with sp^3 carbon via C–C bond formation. The layered BQ-Py showed the absorption over the UV-Vis-NIR region (Supplementary Fig. 1), whereas the BQ-HQ charge-transfer complex has no absorption in the NIR region longer than 850 nm. The spectroscopy suggests that the BQ-Py polymer has not only the complex between the BQ and HQ moieties but also the conjugated framework. The same BQ-Py polymer was synthesized by changes in the molar ratio of BQ and Py. In the present solid-vapor reaction system, the reaction proceeds on the surface of solid BQ crystals upon diffusion of Py vapor. The rates of the two key reactions mainly depend on temperature in this experimental method. In addition, the direct mixing of BQ powder in Py liquid also formed the same products (Supplementary Fig. 3).

The BQ-Py polymer showed the weight loss in the range 500–620 °C on the TG curve because of combustion in air atmosphere (the curve (i) in Fig. 2e). The TG curve was similar to that of a commercial graphene oxide (GO) (the curve (ii) in Fig. 2e). In contrast, the weight loss of a commercial PPy was observed in the range 250–600 °C (the curve (iii) in Fig. 2e). The reference compounds showed the weight loss at the lower temperature, such as 160 °C for BQ monomer and 200 °C for the BQ-HQ complex (the curves (iv) and (v) in Fig. 2e). These results indicate that the successive reactions between BQ and Py generate the polymer network structure. In addition, the remaining monomers and oligomers with low molecular weight are removed by the purification processes. The weight ratio of C, H, N, and O was estimated to be C: H: N: O = 67.47: 2.98: 6.11: 23.44 by elemental analysis (Supplementary Table 1, Supplementary Note 1 and Supplementary Fig. 4). The BQ-Py polymer contained BQ and Py moieties 1.00: 0.675 in molar ratio and 37.5 % of the BQ moiety was in the hydroquinone state (Supplementary Fig. 4 and Supplementary Note 1).

Amorphous layered structure. XRD analysis indicates that the BQ-Py polymer formed the turbostratic layered structure (Fig. 3). The BQ-Py polymer shows the broadened weak peaks around $2\theta = 24.1^\circ$ and 41.7° corresponding to the lattice spacings (d) of

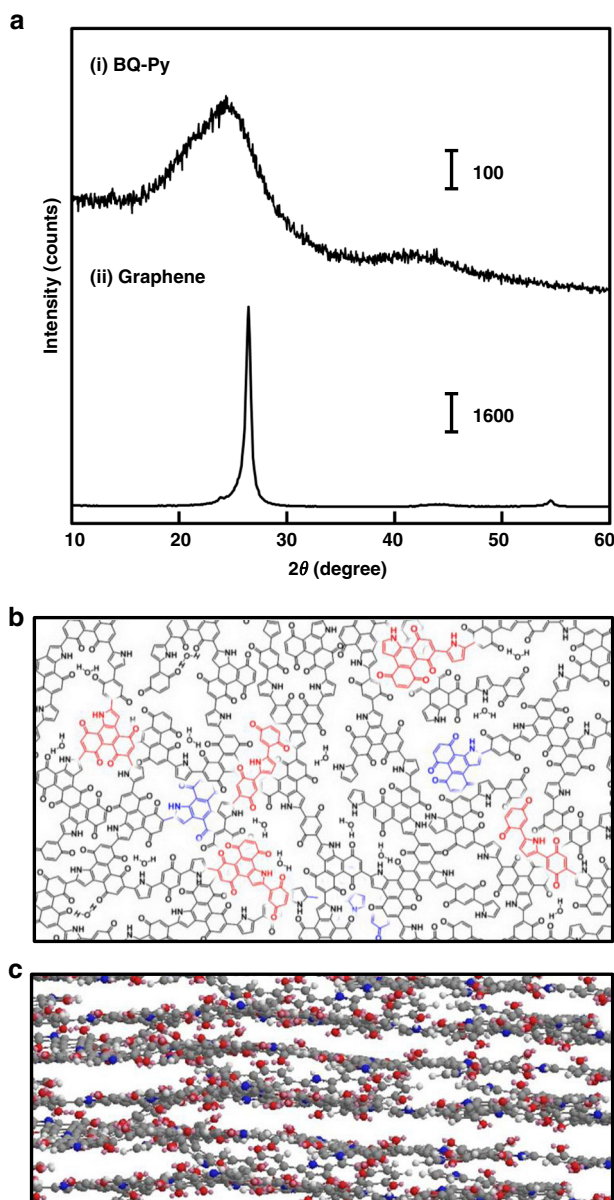


Fig. 3 Schematic illustration of the layered BQ-Py polymer. **a** XRD patterns of the layered BQ-Py polymer (i) and commercial graphene powder (ii). **b, c** Schematic illustration of top (**b**) and side (**c**) views of the layered BQ-Py. The upper and lower layers are grown from the red and blue parts in the panel (**b**), respectively

$d_0 = 0.369$ nm and $d_1 = 0.216$ nm, respectively (the pattern (i) in Fig. 3a). A commercial graphene powder, as a reference, showed the similar peaks around $2\theta = 26.5^\circ$ and $2\theta = 44.0^\circ$ corresponding to $d_0 = 0.336$ and $d_1 = 0.206$ nm, respectively (the pattern (ii) in Fig. 3a). The d_0 is assigned to the interlayer distance of the layered structure. The d_1 is ascribed to the weak periodicity in the planar network consisting of the fused rings. These results suggest that amorphous 2D network forms the turbostratic layered structure (Fig. 3b, c). If the polymerization of BQ and Py proceeds with successive C–C bond formation and pericyclic reaction (Fig. 1a, b), the four types of the structure units, namely the units A–D, can be contained in the network (Fig. 1c). According to the results of elemental analysis (C: H: N: O = 67.47: 2.98: 6.11: 23.44), the units A–D are assumed to be contained in the 2D polymer network with 50: 47: 37: 12 in molar ratio, respectively (Supplementary Fig. 4). On the basis of this structure model, the

calculational weight ratio of C, H, N, and O is estimated to be C: H: N: O = 66.98: 2.49: 6.58: 23.95. The calculational composition is consistent with the experimental one. Figure 3b, c shows the schematic model of the amorphous layered structure synthesized through the consecutive reactions. The electrophilic substitution reaction of BQ on the α position forms a C–C bond with the 2 position of Py (Fig. 1a). The resultant BQ–Py unit has 4π for pericyclic reaction with another BQ as 2π (Fig. 1b). The prior C–C bond formation induces the subsequent pericyclic reaction. The consecutive reactions continued with formation of sp^2 carbon (Fig. 1c). Therefore, the 2D planar layers are obtained by these reaction scheme. If the BQ–Py polymer is comprised of only sp^2 carbons, the layer can possess real 2D structure. However, the BQ moiety induces distortion of the planarity. The plane has slight curvature originating from the BQ moiety (Supplementary Fig. 4). In addition, the interior space is gradually filled with the extended polymer network. The further growth is continued with formation of the upper and lower layers because of the steric repulsion (the red and blue units in Fig. 3b). In this manner, the few-layered structures are spontaneously formed during the synthesis. The growth of the layers and their random stacking induce formation of the amorphous layered material (Fig. 3b, c). This synthetic strategy can be applied to other combinations of the monomers.

Efficient exfoliation of the amorphous layered BQ–Py polymer.

The amorphous layered structure of the BQ–Py polymer was exfoliated into the nanosheets in liquid phase (Fig. 4). The layered BQ–Py polymer was dispersed in water and benzylalcohol under ultrasonic irradiation for 1 h. Then, the dispersion liquid was maintained under stirring at 60°C for 2 days. The BQ–Py nanosheets were observed on the images of transmission electron microscopy (TEM) (Fig. 4a, c). The average lateral size was 751 ± 379 nm and 265 ± 136 nm for the aqueous and benzylalcohol dispersion liquids, respectively (Fig. 4c, g). The layered BQ–Py polymer showed the granular objects 50–200 nm in size in the bulky aggregate on the magnified SEM image before the exfoliation (Supplementary Fig. 5). The SEM images implied that the exfoliated objects are obtained in dispersion media under the appropriate conditions. After the exfoliation, the BQ–Py nanosheets containing the layers were observed on the SEM images (Supplementary Fig. 5). The lateral size of the nanosheets is consistent with that estimated from the TEM images. The FT-IR and Raman spectra were not remarkably changed after the exfoliation into the nanosheets (Supplementary Fig. 5).

The lattice fringes were not clearly observed on the magnified TEM image (Supplementary Fig. 6). Selected-area electron diffraction pattern suggested the presence of the weak periodicity around $d_1 = 0.218$ nm consistent with the XRD analysis (Supplementary Fig. 6). The average thickness was estimated to be 1.62 ± 0.38 nm and 12.26 ± 12.20 nm from the atomic force microscopy (AFM) images of the nanosheets dispersed in aqueous and benzylalcohol media, respectively (Fig. 4b, f and Supplementary Fig. 7). According to the average thickness, the nanosheets contain around 5 and 30 layers for the nanosheets obtained from the aqueous and benzylalcohol dispersions, respectively. The stacked layers were observed on the magnified SEM images of the interior (Supplementary Fig. 5). These observations suggest that the layered BQ–Py polymer is exfoliated into not the monolayered structures but the few-layered structures. The lateral size and thickness were summarized in the histograms (Fig. 4c, g). The difference in the aspect ratio of the nanosheets is ascribed to differences in the affinity between the BQ–Py polymer layers and dispersion media. The results imply that further structure control is achieved by the exfoliation processes, such as types of the

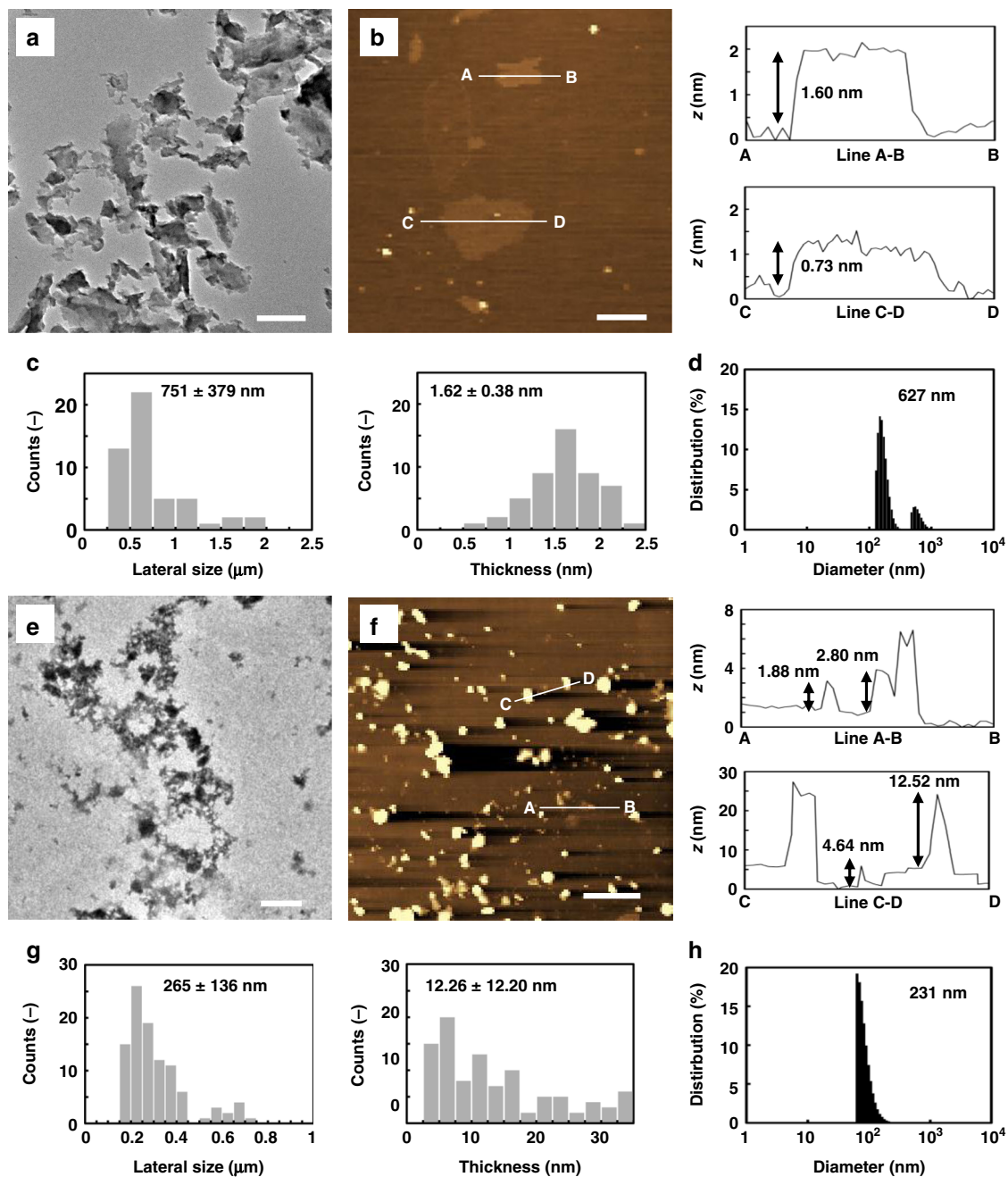


Fig. 4 BQ-Py Nanosheets exfoliated in water (**a-d**) and benzylalcohol (**e-h**). **a, e** TEM images of the BQ-Py nanosheets. **(b, f)** AFM images and its height profiles. **c, g** Histograms of the lateral size and thickness estimated from the TEM and AFM images, respectively. **d, h** Particle-size distribution of the BQ-Py nanosheets estimated from the DLS analysis. The scale bar for (**a, b, e, f**) represents 1 μm

dispersion medium. In our recent work, the lateral size and yield of the exfoliated nanosheets were actually different in the types of the dispersion media¹⁶. This study implied the correlation of the affinity between the interlayer space and dispersion medium with the lateral size. The mechanical stress to the layers is related to the size of the exfoliated nanosheets. Since the higher affinity induces lower stress for exfoliation processes of the layers, the larger lateral size and thinner thickness can be achieved. However, further study is required for understanding the detailed mechanisms and key factors.

The yield of the exfoliation is 43.7% for water and 47.8% for benzylalcohol at 60 °C for 2 days. The calculation method was described in the Methods. The dispersion liquids showed the average particle size 627 nm for water and 231 nm for

benzylalcohol on the particle-size distribution measured by dynamic light scattering (DLS) (Fig. 4d, h). Although these average sizes showed the smaller values than those estimated from the TEM images (Fig. 4a, c, e, g), the distribution suggests the presence of not the aggregated sheets but the dispersed ones in the dispersion liquid. A previous report suggested that size of nanosheets has correlation with the particle size analyzed by DLS⁶⁵. If the unexfoliated powders and/or aggregated nanosheets are dispersed, the peaks is observed in the range larger than 1 μm on the particle-size distribution. These results imply that the particle-size distribution can be used for the screening the exfoliation and dispersion states for the nanosheets. The same particle-size distribution was achieved only after ultrasonic radiation for 1 h without stirring at 60 °C for 2 days

(Supplementary Fig. 8). Moreover, the yield was 24.1% and 44.6% in water and benzylalcohol after the exfoliation for 1 h. This exfoliation efficiency is comparable to other high-efficient exfoliation systems within 1 h in previous works (Supplementary Table 2)^{66–70}. In previous works, the higher exfoliation efficiency is achieved by the specific method and equipment, such as microwave heating in ionic liquid. In contrast, our layered BQ–Py was exfoliated into the nanostructures by just sonication in dispersion medium. Nevertheless, the efficiency of this work is one of the best performances compared with previous works. These results imply that the amorphous nature contributes to efficient exfoliation into the nanosheets.

According to the structure model, the BQ–Py layers have the pore, as shown in Fig. 3b. The interior pore remains as the closed pore in the random stacks of the layers. In fact, gas adsorption–desorption behavior was not observed on the adsorption isotherm (Supplementary Fig. 9 and Supplementary Note 2). Since exfoliation of the layered BQ–Py forms the nanosheets in the dispersion media, the specific surface area for electrochemical reactions is increased after the exfoliation. The surface of the nanosheets was effectively used for reactions, such as sensing, catalytic, and electrochemical applications, in our previous works^{14,38}. The specific surface area is calculated to be $55.1 \text{ m}^2 \text{ g}^{-1}$ and $79.2 \text{ m}^2 \text{ g}^{-1}$, respectively, for the BQ–Py nanosheets dispersed in water and benzylalcohol on the assumption of the average thickness, lateral size, and density same as that of graphite (Supplementary Fig. 9 and Supplementary Note 2).

The BQ–Py polymer showed the redox reactions originating from the quinone moieties on cyclic voltammogram (CV) (Fig. 5). The two redox peaks around 0 V and 0.5 V (vs. Ag/AgCl) are attributed to the anthraquinone (AQ) and BQ moieties, respectively. The presence of these two redox peaks is consistent with the structure model in Fig. 3b. The specific capacity of the layered BQ–Py was 49.7 mA h g^{-1} at 1 mV s^{-1} . The BQ–Py nanosheets showed the improved specific capacity, such as 72.7 mA h g^{-1} and $100.8 \text{ mA h g}^{-1}$ after exfoliation in water and benzylalcohol, respectively (Fig. 5). These facts suggest that the electrochemical surface area mainly originates from not the pores but the nanosheet morphologies. On the other hand, the specific capacitance originating from electric-double-layer capacitance (EDLC) of the BQ–Py nanosheets is estimated to be $<7.19 \text{ mA h g}^{-1}$ from the CV curves of the reduction in the range 0.1–0.2 V without overlapping of the remarkable redox peaks originating from the quinone moieties.

Catalytic performance for HER. The resultant BQ–Py nanosheets showed the enhanced performance as an electrocatalyst for HER (Fig. 6). The BQ–Py nanosheets exhibit Py moiety as the active site on the surface. The catalytic properties of the BQ–Py nanosheets were measured by linear sweep voltammetry (LSV) on glassy carbon (GC) electrode in 0.5 mol dm^{-3} sulfuric acid (H_2SO_4). The BQ–Py nanosheets dispersed in benzylalcohol was coated on GC electrode. Since the BQ–Py polymer contained BQ moieties, the electrochemical reduction from BQ to hydroquinone states was performed to recover the conjugation and ensure the hydrophilicity by chronoamperometry at -0.30 V vs. RHE for 5 h (Supplementary Fig. 10 and Supplementary Note 3). The BQ–Py nanosheets showed current corresponding to HER on the LSV curve in the range 0 to -0.61 V vs. RHE (Fig. 6a). Overpotential for HER (ΔE) was estimated from the LSV curve at the current density -10 mA cm^{-2} . The ΔE was measured to be 0.421 V for the layered BQ–Py polymer before exfoliation and 0.058 V for platinum as a reference (the blue and green solid lines in Fig. 6a). The current density was not achieved to -20 mA cm^{-2}

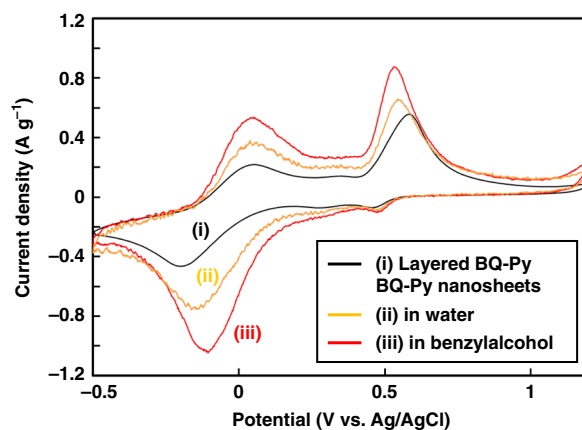


Fig. 5 Electrochemical properties of BQ–Py. CV curves of the layered BQ–Py (i) and nanosheets exfoliated in water (ii) and benzylalcohol (iii)

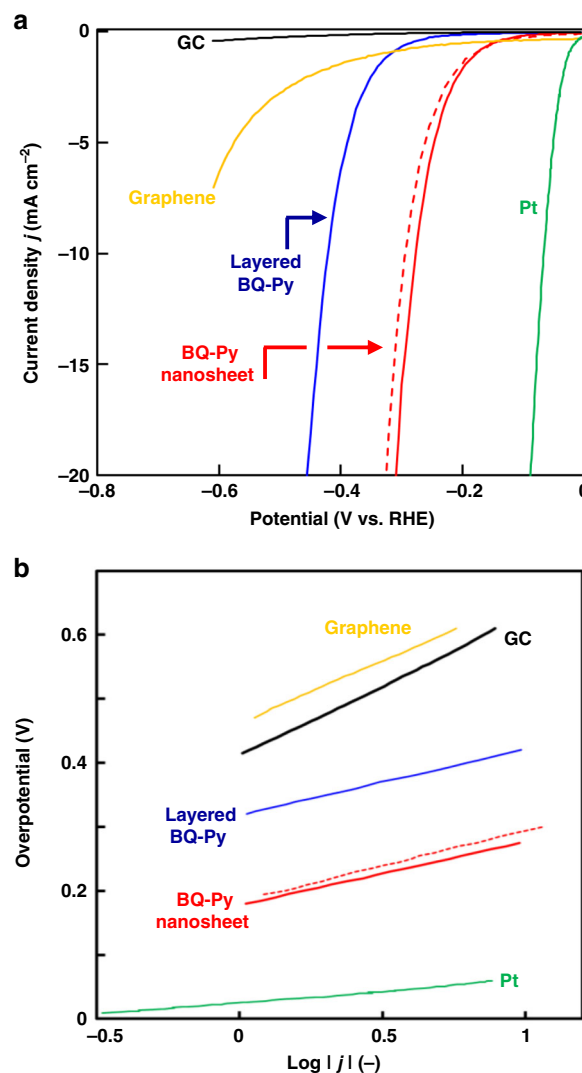


Fig. 6 Application of the BQ–Py polymer as a metal-free electrocatalyst for HER. LSV curves (a) and Tafel slopes (b) of bare GC electrode (black line), commercial graphene (yellow line), the layered BQ–Py (blue line), the BQ–Py nanosheets (red line), and the BQ–Py nanosheets after cyclic voltammetry in the range 0 to -0.3 V (vs. RHE) for 500 cycles (red dashed line)

for bare GC electrode and commercial graphene in this potential range (the black and yellow solid lines in Fig. 6a). The ΔE was decreased to 0.277 V for the BQ–Py nanosheets after the exfoliation (the red solid line in Fig. 6a). The ΔE was reproducible for the different samples, namely average 0.309 ± 0.027 V (number of the samples, $n = 5$) (Supplementary Fig. 10 and Supplementary Note 3). The contamination of the dissolved platinum had no influence on the properties because the similar decrease in the ΔE was observed for the same measurement using graphite counter electrode instead of platinum (Supplementary Fig. 10). Moreover, the ΔE was not changed after the cyclic voltammetry in the range 0 to -0.3 V (vs. RHE) for 500 cycles (the red dashed lines in Fig. 6a and Supplementary Fig. 10). These results indicate that the BQ–Py nanosheets can be used as a superior electrocatalyst for HER with low ΔE and stability. The Tafel slope showed the slope value 98.9 mV dec^{-1} for the BQ–Py nanosheets, $102.5 \text{ mV dec}^{-1}$ for the layered BQ–Py, $219.0 \text{ mV dec}^{-1}$ for bare GC electrode, and 36.3 mV dec^{-1} for Pt electrode (Fig. 6b). The smaller slope value implies the faster electrode kinetics. The decrease in ΔE after the exfoliation is ascribed to an increase in the active site on the nanosheet surface. On the other hand, the Tafel slope was not changed before and after the exfoliation. This result means that the BQ–Py polymer has sufficient hydrophilicity and conductivity for electrochemical HER.

The layered BQ–Py polymer was immersed in 0.5 mol dm^{-3} H_2SO_4 and 0.5 mol dm^{-3} sodium hydroxide (NaOH) aqueous solutions for 5 h to study the stability. The XRD pattern and FT-IR spectrum have no remarkable changes after the acid and base treatments (Supplementary Fig. 11 and Supplementary Note 4). In addition, the morphologies and size of the exfoliated BQ–Py nanosheets were not remarkably changed after the acid and base treatments (Supplementary Fig. 11). The exchange current density and turn-over frequency were comparable to those of heteroatom-doped nanocarbons (Supplementary Fig. 10 and Supplementary Note 3). The present synthetic strategy can be applied to develop a variety of nanocarbons analogs.

The BQ–Py nanosheets showed one of the smallest ΔE and Tafel slope compared with metal-free nanocarbons to the best of our knowledge (Supplementary Table 3, Supplementary Fig. 12 and Supplementary Note 5)^{46–64}. A couple of previous works showed the superior performances, such as graphene with doping of multiple heteroatoms⁴⁸, carbon nitride assembled with graphene^{51,52}, graphene with three-dimensional nanostructures⁵³. However, syntheses of these nanocarbons were performed in the range $400\text{--}1130$ °C (Supplementary Table 3). In contrast, our BQ–Py polymer is synthesized at quite low temperature, namely 60 °C, under ambient pressure. Preparation of the electrocatalyst can be achieved in low energy consumption. Therefore, the BQ–Py nanosheets have the enhanced properties and stability as a metal-free HER electrocatalyst. Further enhancement of the catalytic performance can be achieved by further structure design from molecular to nanometer scales.

Discussion

The spontaneous reactions of BQ and Py in 2D direction induced the formation of the noncrystalline conjugated-polymer layers and their turbostratic stacks at low temperature under ambient pressure. The amorphous layered BQ–Py was efficiently exfoliated into the nanosheets. The resultant BQ–Py nanosheets showed the enhanced performance as a metal-free electrocatalyst for HER. Although previous metal-free HER electrocatalysts are prepared in high temperature processes, the BQ–Py nanoflakes can be prepared at 60 °C under ambient pressure. Our BQ–Py nanosheet may be regarded as a new family of 2D nanocarbons.

Moreover, this work suggests a new strategy to obtain functional organic 2D nanomaterials. Amorphous organic layered materials are synthesized by successive and multiple reactions of target molecules extended into the lateral direction. Their efficient exfoliation provides nanosheets exhibiting the functional units on the surface. The designed organic functional nanosheets realize the enhanced performances and emergent properties.

Methods

Synthesis of BQ–Py polymer. All the reagents were used without purification. Typically, 3.24 g (30 mmol) of BQ powder (1,4-benzoquinone, TCI, 98.0 %) and 2.07 cm^3 (30 mmol) of Py (pyrrole, TCI, 98.0 %) filled in the different glass bottles were set in a closed chamber 250 cm^3 , as shown in Fig. 2a. The reaction was performed in an oven at 60 °C for 48 h under ambient pressure. The resultant black powder in the glass bottle containing BQ was washed with acetone for purification. Then, the powder was dried at 190 °C for 16 h under vacuum condition.

Exfoliation of the layered BQ–Py polymer. The layered BQ–Py polymer, typically 30 mg , was dispersed in 20 cm^3 of purified water and benzylalcohol. The dispersion liquid was set in an ultrasonic bath for 1.5 h and then maintained at 60 °C for 48 h under stirring. The supernatant liquid was collected as the homogeneous dispersion liquid of the BQ–Py nanosheets by decantation. The precipitate was collected as the unexfoliated material by filtration. The weight of the BQ–Py nanosheets (W_{ns}) was measured after drying of the supernatant liquid. The weight of the unexfoliated objects (W_{p}) was also measured after the filtration and drying. The yield (y) was calculated by the following equation (Eq. 1). DLS analysis suggests that the unexfoliated objects and aggregated nanosheets were not included in the supernatant liquid (Fig. 3d, h and Supplementary Fig. 8).

$$y = 100 \times W_{\text{ns}} / (W_{\text{ns}} + W_{\text{p}}) \dots \quad (1)$$

Structure characterization. Crystal structure was analyzed by XRD with Cu-K α radiation (XRD, Bruker, D8 Advance). The powdered sample was set on a silicon sample holder without diffraction peaks in the measured range ($2\theta = 10\text{--}60^\circ$) to lower the background. The molecular structure was analyzed by FT-IR spectroscopy using KBr method (FT-IR, Jasco, FT-IR 4200). TG analysis was performed under air atmosphere (TG, SII TG-DTA 7200). The composition was analyzed by CHN elemental analysis. The bonding states were estimated by XPS (JEOL, JPS-9010TR). ^{13}C NMR spectra of BQ, Py, and layered BQ–Py were measured. The solid-state sample was measured by magic angle spinning method. The morphologies of the layered BQ–Py were observed using a field-emission scanning electron microscopy (FESEM, JEOL, JSM 7600 F). The morphologies of the BQ–Py nanosheets were observed using transmission electron microscopy (TEM, FEI Tecnai G2 Spirit and F20) and atomic force microscopy (AFM, Shimadzu, SPM-9700HT). The dispersion liquid was dropped on a collodion membrane and cleaned silicon substrate for TEM and AFM observations, respectively. The particle-size distribution was measured using DLS (Otsuka electronics, ELSZ-2000ZS). Cyclic voltammetry (Princeton Applied Research, VersaSTAT 3) was measured at a scan rate of 1 mV s^{-1} to determine the structure of the AQ and BQ moieties.

Catalytic activity for HER. The BQ–Py nanosheet dispersed in benzylalcohol was collected after drying. The powder was dispersed in 2-propanol (5 mg cm^{-3}) and the dispersion liquid was put in an ultrasonic bath for 10 min. Then, 0.015 cm^3 of the propanol dispersion liquid was dropped on a glassy carbon electrode (BAS, GCE 002012). The glassy carbon electrode coated with BQ–Py polymer was used as a working electrode. A commercial graphene powder (Fujifilm-Wako, Graphene nanoplatelets aggregates) was also coated on a glassy carbon electrode in the same procedure. Counter and reference electrode were platinum wire (Nilaco, 99.98 %) and Ag/AgCl, respectively. As a reference, the pelletized graphite powder was used instead of platinum counter electrode to confirm no contamination originating from a trace amount of dissolved platinum species. The electrolyte solution was 0.5 mol dm^{-3} sulfuric acid (H_2SO_4 , Kanto, 96.0%). Linear-sweep voltammetry (LSV) was performed in a twin beaker cell in the potential range ($E_{\text{Ag/AgCl}}$) from -0.19 to -0.80 V vs. Ag/AgCl at the scan rate 5 mV s^{-1} (Princeton Applied Research, VersaSTAT 3). The potential was calibrated to that of RHE (E_{RHE}) according to the following equation (Eq. 2):

$$E_{\text{RHE}} = E_{\text{Ag/AgCl}} + 0.0591 \times \text{pH} + 0.199 \dots \quad (2)$$

Prior to the LSV measurement, the BQ–Py polymer was reduced to recovery of the conjugation by chronoamperometry at -0.30 V vs. RHE for 5 h. The stability of the BQ–Py nanosheet for HER was studied using the sample after cyclic voltammetry in the range from 0 to -0.3 V vs. RHE for 500 times at the scan rate 100 mV s^{-1} .

Data availability

All relevant data are available from the authors upon reasonable request.

Received: 18 April 2019 Accepted: 15 July 2019

Published online: 20 August 2019

References

- Nicolosi, V., Chhowalla, M., Kanatzidis, M. G., Strano, M. S. & Coleman, J. N. Liquid exfoliation of layered. *Mater. Sci.* **340**, 1226419 (2013).
- Sakamoto, J., Heijst, Jv, Lukin, O. & Schlüter, A. D. Two-dimensional polymers: just a dream of synthetic chemists? *Angew. Chem. Int. Ed.* **48**, 1030–1069 (2009).
- Wang, Q. & O'Hare, D. Recent advances in the synthesis and application of layered double hydroxide (LDH) nanosheets. *Chem. Rev.* **112**, 4124–4155 (2012).
- Colson, J. W. & Dichtel, W. R. Rationally synthesized two-dimensional polymers. *Nat. Chem.* **5**, 453–465 (2013).
- Cong, H. P., Chen, J. F. & Yu, S. H. Graphene-based macroscopic assemblies and architectures: an emerging material system. *Chem. Soc. Rev.* **43**, 7295–7325 (2014).
- Wang, L. & Sasaki, T. Titanium oxide nanosheets: graphene analogues with versatile functionalities. *Chem. Rev.* **114**, 9455–9486 (2014).
- Osada, M. & Sasaki, T. Two-dimensional dielectric nanosheets: novel nanoelectronics from nanocrystal building blocks. *Adv. Mater.* **24**, 210–228 (2012).
- Lotsch, B. V. Vertical 2D heterostructures. *Ann. Rev. Mater. Res.* **45**, 85–109 (2015).
- Mendoza-Sánchez, B. & Gogotsi, Y. Synthesis of two-dimensional materials for capacitive energy storage. *Adv. Mater.* **28**, 6104–6135 (2016).
- Ariga, K., Watanabe, S., Mori, T. & Takeya, J. Soft 2D nanoarchitectonics. *NPG Asia Mater.* **10**, 90–106 (2018).
- Khan, A. H. et al. Two-dimensional (2D) nanomaterials towards electrochemical nanoarchitectonics in energy-related applications. *Bull. Chem. Soc. Jpn.* **90**, 627–648 (2017).
- Backes, C. et al. Guidelines for exfoliation, characterization and processing of layered materials produced by liquid exfoliation. *Chem. Mater.* **29**, 243–255 (2017).
- Ma, R. & Sasaki, T. Two-dimensional oxide and hydroxide nanosheets: controllable high-quality exfoliation, molecular assembly, and exploration of functionality. *Acc. Chem. Res.* **48**, 136–143 (2015).
- Honda, M., Oaki, Y. & Imai, H. Hydrophobic inorganic–organic composite nanosheets based on monolayers of transition metal oxides. *Chem. Mater.* **26**, 3579–3585 (2014).
- Ishijima, Y., Okaniwa, M., Oaki, Y. & Imai, H. Two exfoliation approaches for organic layered compounds: hydrophilic and hydrophobic polydiacetylene nanosheets. *Chem. Sci.* **8**, 647–653 (2017).
- Nakada, G., Igarashi, Y., Imai, H. & Oaki, Y. Materials-informatics-assisted high-yield synthesis of 2D nanomaterials through exfoliation. *Adv. Theory Simul.* **2**, 1800180 (2019).
- Waller, P. J., Gándara, F. & Yaghi, O. M. Chemistry of covalent organic frameworks. *Acc. Chem. Res.* **48**, 3053–3063 (2015).
- Xiang, Z., Cao, D. & Dai, L. Well-defined two dimensional covalent organic polymers: rational design, controlled syntheses, and potential applications. *Polym. Chem.* **6**, 1896–1911 (2015).
- Sun, Q., Aguila, B. & Ma, S. A bifunctional covalent organic framework as an efficient platform for cascade. *Catal. Mater. Chem. Front.* **1**, 1310–1316 (2017).
- Meng, Y., Lin, G., Ding, H., Liao, H. & Wang, C. Impregnation of sulfur into a 2D pyrene-based covalent organic framework for high-rate lithium–sulfur batteries. *J. Mater. Chem. A* **6**, 17186–17191 (2018).
- Antonietti, M. & Oschatz, M. The concept of “noble, heteroatom-doped carbons,” their directed synthesis by electronic band control of carbonization, and applications in catalysis and energy materials. *Adv. Mater.* **30**, 1706836 (2018).
- Zhuang, X., Mai, Y., Wu, D., Zhang, F. & Feng, X. Two-dimensional soft nanomaterials: a fascinating world of materials. *Adv. Mater.* **27**, 403–427 (2015).
- Liu, H. et al. Synthesis and mechanical exfoliation of imine-linked two-dimensional conjugated polymers. *J. Mater. Chem. C* **6**, 722–726 (2018).
- Liu, J., Lyu, P., Zhang, Y., Nachtigall, P. & Xu, Y. New layered triazine framework/exfoliated 2d polymer with superior sodium-storage properties. *Adv. Mater.* **30**, 1705401 (2018).
- Peng, P. et al. In situ charge exfoliated soluble covalent organic framework directly used for Zn–Air flow battery. *ACS Nano* **13**, 878–884 (2019).
- Liu, W. et al. Amorphous cobalt–iron hydroxide nanosheet electrocatalyst for efficient electrochemical and photo-electrochemical oxygen evolution. *Adv. Funct. Mater.* **27**, 160394 (2017).
- Liu, T. et al. 2D amorphous iron phosphate nanosheets with high rate capability and ultra-long cycle life for sodium ion batteries. *J. Mater. Chem. A* **4**, 4479–4484 (2016).
- Bennett, T. D. et al. Structure and properties of an amorphous metal-organic framework. *Phys. Rev. Lett.* **104**, 115503 (2010).
- Bennett, T. D. & Cheetham, A. K. Amorphous metal–organic frameworks. *Acc. Chem. Res.* **47**, 1555–1562 (2014).
- Ueyama, D., Horike, S., Inukai, M., Itakura, T. & Kitagawa, S. Reversible solid-to-liquid phase transition of coordination polymer crystals. *J. Am. Chem. Soc.* **37**, 864–870 (2015).
- Zhao, Y., Lee, S. Y., Becknell, N., Yaghi, O. M. & Angell, C. A. Nanoporous transparent MOF glasses with accessible internal surface. *J. Am. Chem. Soc.* **138**, 10818–10821 (2016).
- Selvamani, V. et al. High rate performing in situ nitrogen enriched spherical carbon particles for Li/Na-Ion cells. *ACS Appl. Mater. Interfaces* **9**, 39326–39336 (2017).
- Li, Y. et al. Conductive microporous covalent triazine-based framework for high-performance electrochemical capacitive energy storage. *Angew. Chem. Int. Ed.* **57**, 7992–7996 (2018).
- Khayum, M. A. et al. Chemically delaminated free-standing ultrathin covalent organic nanosheets. *Angew. Chem. Int. Ed.* **55**, 15604–15608 (2016).
- Wendlandt, A. E. & Stahl, S. S. Quinone-catalyzed selective oxidation of organic molecules. *Angew. Chem. Int. Ed.* **54**, 14638–14658 (2015).
- Song, Z. & Zhou, H. Towards sustainable and versatile energy storage devices: an overview of organic electrode materials. *Energy Environ. Sci.* **6**, 2280–2301 (2013).
- Sato, K., Arayasu, M., Masaki, H., Imai, H. & Oaki, Y. Hierarchical bicontinuous structure of redox-active organic composites and their enhanced electrochemical properties. *Chem. Commun.* **53**, 7329–7332 (2017).
- Oaki, Y. & Sato, K. Crystal-controlled polymerization: recent advances in morphology design and control of organic polymer materials. *J. Mater. Chem. A* **6**, 23197–23219 (2018).
- Prasad, K. K. A reinvestigation of the reaction of indole with 1,4-quinones. *Tetrahedron Lett.* **15**, 1361 (1974).
- Lion, C. et al. Reaction of pyrroles with naphthoquinones. Synthesis of new pyrrolynaphthoquinone dyes. *J. Heterocycl. Chem.* **37**, 1635–1640 (2000).
- Zhang, J., Chen, G., Müllen, K. & Feng, X. Carbon-rich nanomaterials: fascinating hydrogen and oxygen electrocatalysts. *Adv. Mater.* **30**, 1800528 (2018).
- Navalon, S., Dhakshinamoorthy, A., Alvaro, M., Antonietti, M. & García, H. Active sites on graphene-based materials as metal-free catalysts. *Chem. Soc. Rev.* **46**, 4501–4529 (2017).
- Zeng, M. & Li, Y. Recent advances in heterogeneous electrocatalysts for the hydrogen evolution reaction. *J. Mater. Chem. A* **3**, 14942–14962 (2015).
- Duan, J., Cheng, S., Jaroniec, M. Z. & Qiao, S. Single and multiple doping in graphene quantum dots: unraveling the origin of selectivity in the oxygen reduction reaction. *ACS Catal.* **5**, 5207–5234 (2015).
- Rao, C. N. R. & Chhetri, M. Borocarbonitrides as metal-free catalysts for the hydrogen evolution reaction. *Adv. Mater.* **31**, 1803668 (2019).
- Patra, B. C. et al. A metal-free covalent organic polymer for electrocatalytic hydrogen evolution. *ACS Catal.* **7**, 6120–6127 (2017).
- Deng, B. et al. Amine group induced high activity of highly torn amine functionalized nitrogen-doped graphene as the metal-free catalyst for hydrogen evolution reaction. *Carbon* **138**, 169–178 (2018).
- Ito, Y. et al. Correlation between chemical dopants and topological defects in catalytically active nanoporous graphene. *Adv. Mater.* **28**, 10644–10651 (2016).
- Zhao, X., Li, S., Cheng, H., Schmidt, J. & Thomas, A. Ionic liquid-assisted synthesis of mesoporous carbons with surface-enriched nitrogen for the hydrogen evolution reaction. *ACS Appl. Mater. Interfaces* **10**, 3912–3920 (2018).
- Zhou, J. et al. Uniform nanoporous graphene sponge from natural polysaccharides as a metal-free electrocatalyst for hydrogen generation. *J. Mater. Sci.* **53**, 7767–7777 (2018).
- Zheng, Y. et al. Hydrogen evolution by a metal-free electrocatalyst. *Nat. Commun.* **5**, 3783 (2014).
- Zhao, Y. et al. Graphitic carbon nitride nanoribbons: graphene-assisted formation and synergic function for highly efficient hydrogen evolution. *Angew. Chem. Int. Ed.* **53**, 13934–13939 (2014).
- Wang, H. et al. Three-dimensional graphene networks with abundant sharp edge sites for efficient electrocatalytic hydrogen evolution. *Angew. Chem. Int. Ed.* **57**, 192–197 (2018).
- Shinde, S. S., Sami, A. & Lee, J. H. Nitrogen- and phosphorus-doped nanoporous graphene/graphitic carbon nitride hybrids as efficient electrocatalysts for hydrogen evolution. *ChemCatChem* **7**, 3873–3880 (2015).

55. Liu, X. et al. Nitrogen and sulfur co-doped porous carbon derived from human hair as highly efficient metal-free electrocatalysts for hydrogen evolution reactions. *J. Mater. Chem. A* **3**, 8840–8846 (2015).
56. Liu, X. et al. Functional materials from nature: honeycomb-like carbon nanosheets derived from silk cocoon as excellent electrocatalysts for hydrogen evolution reaction. *Electrochim. Acta* **215**, 223–230 (2016).
57. Duan, J., Chen, S., Jaroniec, M. & Qiao, S. Z. Porous C₃N₄ nanolayers@N-graphene films as catalyst electrodes for highly efficient hydrogen evolution. *ACS Nano* **9**, 931–940 (2015).
58. Liu, Y. et al. Efficient and durable hydrogen evolution electrocatalyst based on nonmetallic nitrogen doped hexagonal carbon. *Sci. Rep.* **4**, 6843 (2014).
59. Wei, L. et al. A high-performance metal-free hydrogen evolution reaction electrocatalyst from bacterium derived carbon. *J. Mater. Chem. A* **3**, 7210–7214 (2015).
60. Zhao, Y. et al. Graphitic carbon nitride nanoribbons: graphene-assisted formation and synergic function for highly efficient hydrogen evolution. *Angew. Chem. Int. Ed.* **54**, 13934–13939 (2014).
61. Shinde, S. S., Sami, A. & Lee, J. H. Electrocatalytic hydrogen evolution using graphitic carbon nitride coupled with nanoporous graphene co-doped by S and Se. *J. Mater. Chem. A* **3**, 12810–12819 (2015).
62. Gong, K., Du, F., Xia, Z., Durstock, M. & Dai, L. Nitrogen-doped carbon nanotube arrays with high electrocatalytic activity for oxygen reduction. *Science* **323**, 760–764 (2009).
63. Tabassum, H., Zou, R., Mahmood, A., Liang, Z. & Guo, S. A catalyst-free synthesis of B, N co-doped graphene nanostructures with tunable dimensions as highly efficient metal free dual electrocatalysts. *J. Mater. Chem. A* **4**, 16469–16475 (2016).
64. Chherti, M., Maitra, S., Chakraborty, H., Waghmare, U. V. & Rao, C. N. R. Superior performance of borocarbonitrides, BxCyNz, as stable, low-cost metal-free electrocatalysts for the hydrogen evolution reaction. *Energy Environ. Sci.* **9**, 95–101 (2016).
65. Lotya, M., Rakovich, A., Donegan, J. F. & Coleman, J. N. Measuring the lateral size of liquid-exfoliated nanosheets with dynamic light scattering. *Nanotechnology* **24**, 265703 (2013).
66. Tong, J. et al. Rapid and high-yield production of g-C₃N₄ nanosheets via chemical exfoliation for photocatalytic H₂ evolution. *Rsc. Adv.* **5**, 88149–88153 (2015).
67. Matsumoto, M., Saito, Y., Park, C., Fukushima, T. & Aida, T. Ultrahigh-throughput exfoliation of graphite into pristine ‘single-layer’ graphene using microwaves and molecularly engineered ionic liquids. *Nat. Chem.* **7**, 730–736 (2015).
68. Zheng, J. et al. High yield exfoliation of two-dimensional chalcogenides using sodium naphthalenide. *Nat. Commun.* **4**, 2995 (2014).
69. Lin, H. et al. Rapid and highly efficient chemical exfoliation of layered MoS₂ and WS₂. *J. Alloy. Compd.* **699**, 222–229 (2017).
70. Zhao, S. et al. Green and high-efficiency production of graphene by tannic acid-assisted exfoliation of graphite in water. *ACS Sustain. Chem. Eng.* **6**, 7652–7661 (2018).

Acknowledgements

This work is partially supported by Sekisui Chemical Nature Research Program (Y.O.), JST PRESTO (JPMJPR16N2) (Y.O.), and ENEOS Hydrogen Trust Fund (Y.O.). One of the authors (K.S.) is grateful for a JSPS research fellowship for young scientists (16J03122).

Author contributions

S.Y., K.S., and Y.O. conceived and designed the experiments; S.Y., K.S., J.S. performed the experiments; K.S. and Y.O. supported the experiments; S.Y., K.S., J.S., H.I., and Y.O. discussed the results and wrote the paper.

Additional information

Supplementary information accompanies this paper at <https://doi.org/10.1038/s42004-019-0201-9>.

Competing interests: The authors declare no competing interests.

Reprints and permission information is available online at <http://npg.nature.com/reprintsandpermissions/>

Publisher's note: Springer Nature remains neutral with regard to jurisdictional claims in published maps and institutional affiliations.



Open Access This article is licensed under a Creative Commons Attribution 4.0 International License, which permits use, sharing, adaptation, distribution and reproduction in any medium or format, as long as you give appropriate credit to the original author(s) and the source, provide a link to the Creative Commons license, and indicate if changes were made. The images or other third party material in this article are included in the article's Creative Commons license, unless indicated otherwise in a credit line to the material. If material is not included in the article's Creative Commons license and your intended use is not permitted by statutory regulation or exceeds the permitted use, you will need to obtain permission directly from the copyright holder. To view a copy of this license, visit <http://creativecommons.org/licenses/by/4.0/>.

© The Author(s) 2019